Materials Science & Engineering A 857 (2022) 144085

Contents lists available at ScienceDirect

Materials Science & Engineering A

journal homepage: www.elsevier.com/locate/msea

Achieving better synergy of strength and ductility by adjusting size and volume fraction of coherent κ'–carbides in a lightweight steel

Jian Wang [a,b], Muxin Yang [a], Xiaolei Wu [a,b], Fuping Yuan [a,b,*]

[a] State Key Laboratory of Nonlinear Mechanics, Institute of Mechanics, Chinese Academy of Science, 15 Beisihuan West Road, Beijing, 100190, China
[b] School of Engineering Science, University of Chinese Academy of Sciences, 19A Yuquan Road, Beijing, 100049, China

ARTICLE INFO

Keywords:
Lightweight steel
Heterogeneous grain structure
Nanoprecipitate
Ductility
Geometrically necessary dislocation
Precipitation hardening

ABSTRACT

Heterogeneous grain structures with dual-nanoprecipitates have been designed and fabricated in a lightweight steel. The size and the volume fraction of coherent κ'–carbides are increased by aging treatment, while the volume fraction of B2 precipitates and the heterogeneous grain structure are nearly unchanged after aging treatment. The aged samples are found to have a better synergy of strength and ductility, as compared to the unaged samples. The better tensile properties in the aged samples can be owing to the higher hetero-deformation-induced hardening and the higher density of induced geometrically necessary dislocations during tensile deformation. Two distinct precipitation hardening mechanisms are revealed for the dual-nanoprecipitates, i.e., bypassing mechanism for B2 precipitates and shearing mechanism for coherent κ'–carbides. Numerous dislocations can be observed both around and inside coherent κ'–carbides. High density of stacking faults and nanotwins can also be found in the grain interiors of the aged samples, resulting in strong strain hardening by interaction between them and dislocations. The better tensile properties in the aged samples can also be attributed to the stronger shearing precipitation hardening effect by larger size and higher volume fraction of coherent κ'–carbides.

1. Introduction

Lightweight steels with high performance, such as high strength, large ductility and high fracture toughness, are generally needed and attractive for industrial applications [1–20]. Compared to conventional steels, the lightweight steels with Fe-Mn-Al-C system have attracted extensive research interests since the addition of Al can be effective on both weight reduction and achieving excellent mechanical properties [1,2,4–10,13,15–19]. A good combination of strength and ductility can be achieved in the Fe-Mn-Al-C lightweight steels with nanosized $L'1_2$ κ–carbides [4]. The precipitation hardening mechanisms (shearing or bypassing) for coherent κ–carbides are dependent on the size of coherent κ–carbides. The nanosized coherent κ–carbides could be sheared under high stresses to produce weak hardening and cause local strain softening/localization on one hand, could become incoherent at grain boundaries to promote crack initiation and embrittlement on the other hand [18,21]. Therefore, non-shearable incoherent B2 particles were introduced into the Fe-Mn-Al-C lightweight steels for further improving the tensile properties [16,17], and the hard B2 particles can provide strong strain hardening by bypassing precipitation hardening mechanisms. However, large volume fraction of B2 particles are required for high yield strength, which is generally accompanied by a significant loss of ductility due to the intrinsically brittle nature of the B2 particles [16,17]. Moreover, the size of B2 particles was hardly to be controlled in nanoscale.

Recently, a novel approach with the concept of a dual-nanoprecipitation (both κ–carbides and B2 particles) was introduced into Fe-Mn-Al-Ni-C lightweight steels, and superior tensile properties were achieved in these steels [19,22]. In these steels, both shearing and bypassing mechanisms could be operative, B2 particles could inhibit the local strain softening and both precipitates could help to nucleate in grain interiors for each other. Better tensile properties can be obtained in these steels by optimizing the benefits from nanoprecipitates [19,22–28].

The low yield strength for metals and alloys with coarse grains (CGs) generally limits their practical applications, and such limitation can be resolved by grain boundary strengthening and dislocation strengthening [29,30]. However, the strength enhancement by these two mechanisms

* Corresponding author. State Key Laboratory of Nonlinear Mechanics, Institute of Mechanics, Chinese Academy of Science, 15 Beisihuan West Road, Beijing, 100190, China.
E-mail address: fpyuan@lnm.imech.ac.cn (F. Yuan).

https://doi.org/10.1016/j.msea.2022.144085
Received 15 August 2022; Received in revised form 22 September 2022; Accepted 22 September 2022
Available online 29 September 2022

in homogeneous structures is generally accompanied with the reduction in ductility. Heterogeneous grain structures [31–33] and gradient structures [34–38] have been proven to be effective in obtaining excellent synergy of strength and ductility due to the hetero-deformation-induced (HDI) hardening [39,40]. HDI hardening can be induced by the strain gradients and geometrically necessary dislocations (GNDs) at the boundaries between hard/soft domains. Thus, even better tensile properties could be obtained in the aforementioned steels with dual-nanoprecipitation by deploying heterogeneous grain structures.

While, how the dual-nanoprecipitates and heterogeneous grain structures affect the strain hardening behaviors and the tensile properties is still an open question. Specially, the size and volume fraction of the coherent nanosize κ–carbides could be tailored to further improve the mechanical properties. In the present study, heterogeneous grain structures with dual-nanoprecipitates were deployed in a Fe-29.02Mn-8.76Al-4.99Ni-1.04C (wt.%) steel by cold rolling and subsequent annealing, and excellent tensile properties were obtained in this lightweight steel. Moreover, we have shown that better synergy of strength and ductility can be achieved by adjusting the size and volume fraction of the coherent nanosize κ–carbides through aging treatment after annealing, and the corresponding mechanisms have been revealed through the detailed microstructure characterizations.

2. Materials and experimental procedures

The Fe-29.02Mn-8.76Al-4.99Ni-1.04C (wt.%) steel was cast and remelted several times by an induction furnace under protection of Ar atmosphere. The as-cast ingots were then homogenized at 1473 K for 2 h, followed by water quenching. The ingots were hot-rolled at a starting temperature of 1373 K into 4 mm thick plates, followed by cold-rolling with a thickness reduction of 60%. The cold-rolling plates were annealed at various temperatures (1073, 1173 K for 3 min, 1273, 1373 K for 30 min) under vacuum conditions, followed by fast cooling, these samples are named AN1073, AN1173, AN1273 and AN1373. Some samples were then aged at 873 K for 30min, and these sample are referred as AG1173, AG1273 and AG1373.

The gauge dimensions of dog-bone specimens for quasi-static tensile testing were set to be 18 × 2.5 × 1 mm^3. The uniaxial tensile tests and the load-unload-reload (LUR) tests were performed with an engineering strain rate of 5 × 10^{-4}/s and at room temperature under displacement control utilizing an MTS landmark testing machine. The tensile loading direction was along the rolling direction, and the displacement was controlled and measured by an extensometer during tensile deformation. The other details for LUR tests can be found in our previous paper [31,32]. Electron backscattered diffraction (EBSD), transmission electron microscope (TEM) and high-resolution TEM (HRTEM) were used to characterize the microstructures prior to and after tensile testing. X-ray diffraction (XRD) was used to reveal the phases and the volume fraction for each phase. Energy disperse spectroscopy (EDS) was utilized to characterize the element distributions. The other details for EBSD, TEM, HRTEM, XRD, and EDS observations and sample preparations can be referred to the previous research [33,41].

3. Results

3.1. Microstructure characterizations prior to tensile testing

The heterogeneous grain structures have been characterized by EBSD observations. The images of inverse pole figure (IPF) for the samples of AN1073, AN1173 and AG1173 are shown in Fig. 1. In Fig. 1, the un-recrystallized areas are defined when a value of grain reference orientation deviation (GROD) is greater than 5^0. These un-recrystallized areas still show a deformation band feature by cold-rolling, and while the recrystallized areas display equi-axed grains. Thus these three samples can all be considered as heterogeneous grain structures since both un-recrystallized areas and recrystallized grains exist. The volume fractions of the recrystallized areas are estimated to be about 4.1%, 59.6% and 47.3% for the samples of AN1073, AN1173 and AG1173, respectively. These observations indicate that the volume fraction of the recrystallized areas increases with increasing annealing temperature, while aging treatment has little effect on the heterogeneous grain structures, only altering the size and volume fraction of nano-precipitates, as shown later on.

XRD spectra for the AN1073, AN1173 and AG1173 samples are displayed in Fig. 2a. The peaks for both the FCC phase and the B2 phase can be clearly observed. While, the peaks of the austenite phase and the κ'–carbides are overlapped since they are coherent. Utilizing the (220) diffraction peaks as examples in the close-up view of Fig. 2b, it is clearly shown that these (220) peaks are asymmetric. Thus, the asymmetric overlapped (220) peaks were separated into two peaks for the austenite phase and the coherent κ'–carbides utilizing the Gaussian fitting (Fig. 2b). Then, the volume fractions of various phases can be calculated using the integrated areas of diffraction peaks. The volume fractions of B2 phase were estimated to be about 3.83%, 2.74% and 3.16% for the AN1073, AN1173 and AG1173 samples, respectively. These observations indicate that the volume fraction of B2 phase is nearly unchanged after aging treatment. The relative volume fractions of coherent κ'–carbides in the austenite matrix were calculated to be about 32.1%, 24.7% and 42.0% for the AN1073, AN1173 and AG1173 samples, respectively. Thus the relative volume fraction of coherent κ'–carbides in the austenite matrix increases significantly after aging treatment. The phase map by EBSD for the AG1173 sample is shown in Fig. 2c, in which both FCC phase and B2 phase can be identified. In the EBSD phase map, the B2 precipitates can be found mostly at the positions of GBs and triple-junctions, only a few B2 precipitates can be observed in the grain interiors. The austenite phase and the coherent κ'–carbides can't be differentiated by EBSD due to the coherent relationship, and these two phases will be carefully characterized by TEM and HRTEM observations later on. The B2 nanoprecipitates can also be observed in the grain interiors by the bright-field TEM images, as indicated in Fig. 2d. Based on the EBSD observations, the average size and the volume fraction of B2 precipitates at GBs and triple-junctions is estimated to be about 227 nm and about 1.85%. This estimated volume fraction for B2 phase by EBSD is much smaller than that obtained by XRD, since the B2 nano-precipitates with much smaller size can't be identified by EBSD and can only be observed by TEM images.

The microstructures for the AN1173 and AG1173 samples were

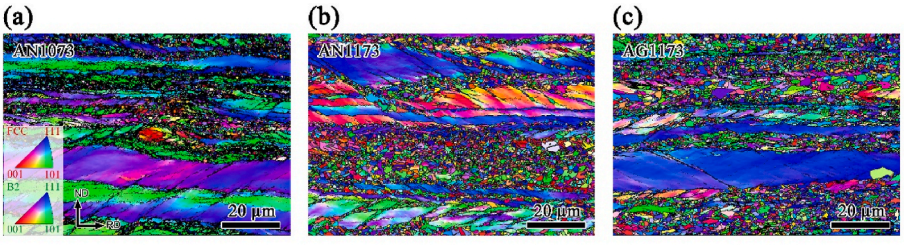

Fig. 1. EBSD observations for selected samples. IPF images for (a) the AN1073 sample; (b) the AN1173 sample; (c) the AG1173 sample.

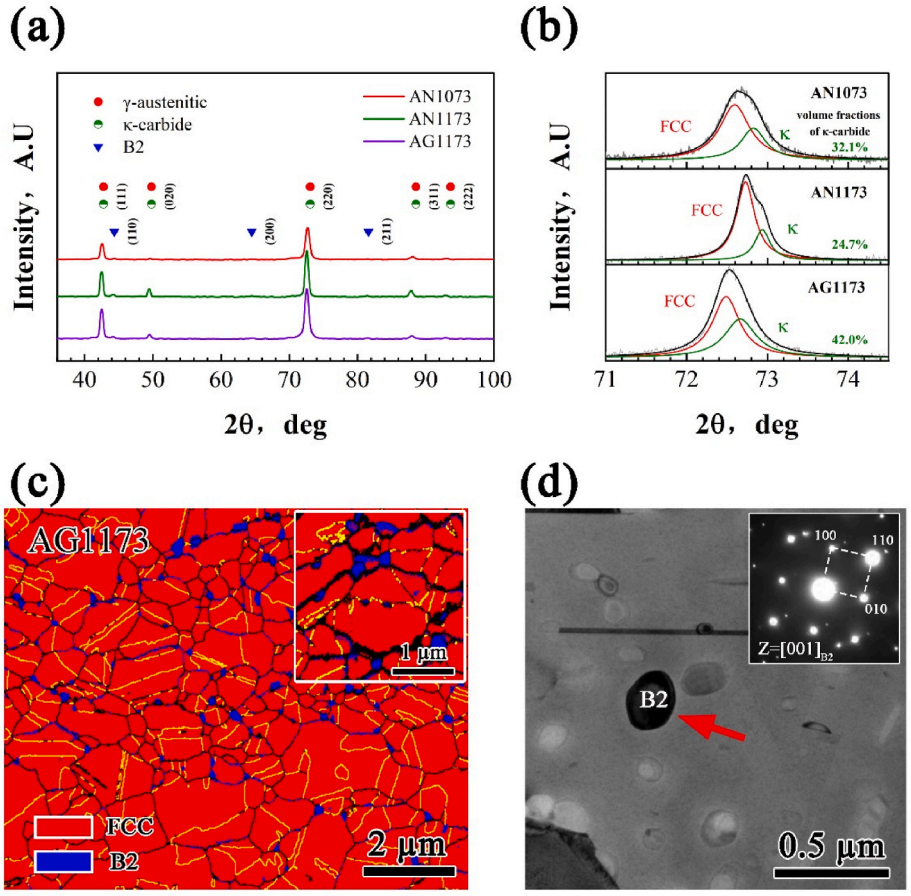

Fig. 2. (a) XRD spectra for the AN1173 and AG1173 samples. (b) The asymmetric overlapped (220) peak and the separated two peaks for the austenite phase and the coherent κ'–carbides utilizing the Gaussian fitting. (c) The phase map by EBSD for the AG1173 sample. (d) Bright-field TEM image for the AG1173 sample showing smaller B2 precipitates.

further characterized by TEM observations, as shown in Fig. 3. The bright-field TEM images for these two samples are displayed in Fig. 3a and c. Both recrystallized CGs and un-recrystallized areas are observed for these two samples, and the dislocation density is found to be very low for the recrystallized CGs. Most of B2 nanoprecipitates with smaller size are in the austenite grain interiors, instead of at GBs, should have

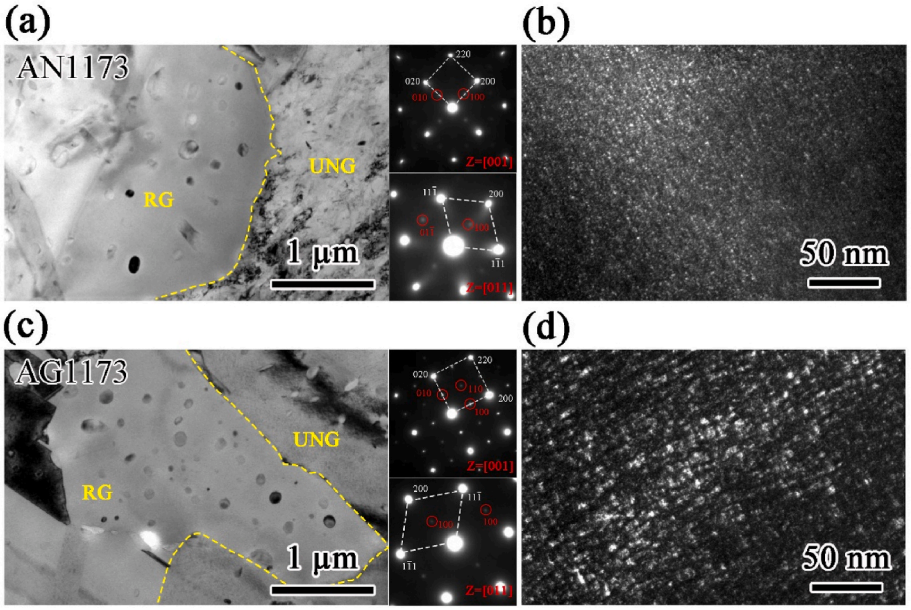

Fig. 3. TEM observations for (a) (b) the AN1173 sample and (c) (d) the AG1173 samples. Bright-field images are given in (a) and (c), while dark-field images are shown in (b) and (d). The coherent κ'–carbides can be identified by the SAED in the insets.

benefits for better tensile ductility. Based on TEM observations, the average sizes of B2 nanoprecipitates were calculated to be about 78 nm and 63 nm for the AN1173 sample and the AG1173 sample, respectively. The volume fractions of B2 nanoprecipitates with smaller size were estimated to be about 0.56% and 0.84% based on these TEM images for the AN1173 sample and the AG1173 sample, respectively. Thus the total volume fractions of B2 phase based on both EBSD and TEM should be about 2.41% and 3.48% for the AN1173 sample and the AG1173 sample respectively, which are consistent with the previous XRD results. Based on the dark-field TEM images in Fig. 3b and d, the average sizes of the coherent κ'–carbides are found to increase from about 2.25 nm to 4.33 nm, and the corresponding relative volume fractions are observed to increase from about 22.9% to 37.2% for the AG1173 sample, as compared to the AN1173 sample. These observations further confirm

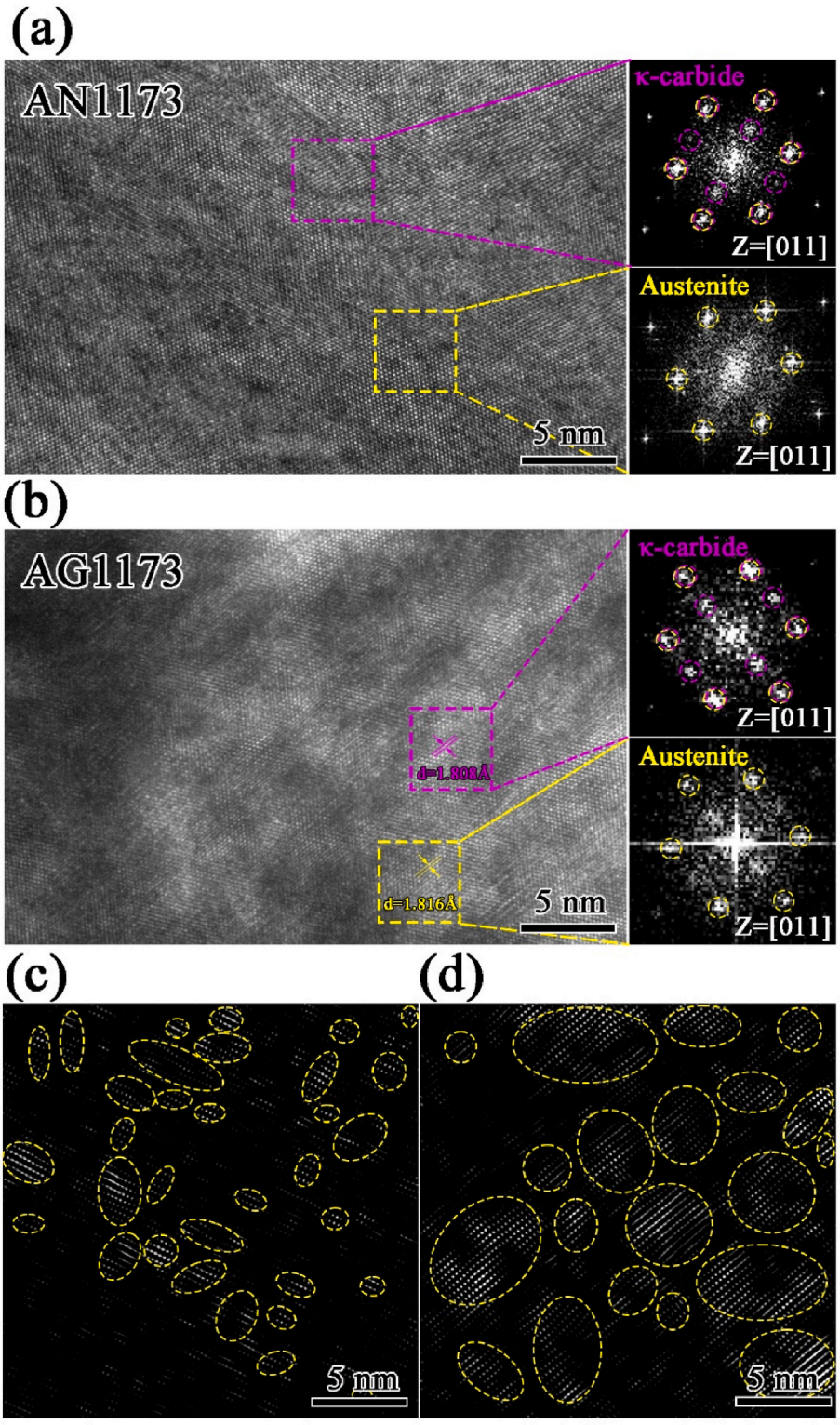

Fig. 4. HRTEM images showing the coherent κ'–carbides for (a) the AN1173 sample and (b) the AG1173 sample. The corresponding images after FFT and inverse FFT for (c) the AN1173 sample and (d) the AG1173 sample.

that the aging treatment has little effect on the grain structure of austenite phase and on the size and volume fraction of B2 phase, while produces larger size and much higher volume fraction for the coherent κ'–carbides. The formation temperature for the B2 phase is relatively high, thus the volume fractions of the B2 phase remain nearly unchanged during aging treatment (873 K).

The coherent κ'–carbides in the austenite matrix are also characterized carefully by HRTEM images, as indicated in Fig. 4. The HRTEM images for the AN1173 sample and the AG1173 sample are displayed in Fig. 4a and b respectively, and the insets show the corresponding images after fast Fourier transform (FFT) for the rectangular areas. Thus, both austenite phase and coherent κ'–carbides can be identified by the images after FFT. Moreover, the images after FFT and inverse FFT for the AN1173 sample and the AG1173 sample are displayed in Fig. 4c and d respectively. In Fig. 4c and d, the coherent κ'–carbides are identified and circled by yellow dash lines. The average sizes of coherent κ'–carbides are estimated to be about 2.15 nm and 3.97 nm, and the volume fractions of coherent κ'–carbides are calculated to be about 21.8%–36.8%, for the AN1173 sample and the AG1173 sample, respectively. These results by HRTEM observations are consistent with the aforementioned results by dark-field TEM images. These observations further confirm that the aged samples have larger size and higher volume fraction of coherent κ'–carbides as compared to the unaged samples.

Elements distributions in nanoprecipitates are characterized by EDS mapping. Fig. 5 shows EDS mappings of an area with several B2 particles for the AG1173 sample. Moreover, the concentration distributions for various elements along the marked line in Fig. 5a are also displayed in Fig. 5b. It is clearly shown that Al and Ni elements are highly enriched in the B2 phase, while Fe and Mn elements are deprived in the B2 particles, these observations are consistent with the previous paper [19]. Previous study also shows that C element is highly enriched and Fe element is slightly deprived in the coherent κ'–carbides as compared to the austenite matrix [19].

3.2. Tensile properties and HDI hardening

The tensile properties for all samples in the present study are displayed in Fig. 6. The engineering stress-strain curves for selected samples (AN1073, AN1173, AN1273, AN1373, AG1173, AG1273 and AG1373) are shown in Fig. 6a, while the corresponding curves of hardening rate and true stress as a function of true strain are displayed in Fig. 6b. As compared to the unaged samples, the corresponding aged samples have a higher yield strength, but a smaller uniform elongation. While, the aged sample of AG1173 has a much larger uniform elongation with a similar yield strength, as compared to the sample annealed at a lower temperature (AN1073). As shown in Fig. 5b, the highest hardening rate and an up-turn phenomenon are observed in the AN1173 sample. It is also interesting to note that the AG1173 sample shows a higher hardening rate and a small up-turn phenomenon at the similar yield strength level as compared to the AN1073 sample, resulting in better tensile ductility. The up-turn phenomenon can be partly attributed to the HDI hardening. But other issues (yield strength, mobile dislocation density, etc.) can also be related to the up-turn phenomenon [42]. The decrease of work hardening capability after aging (AG1173 vs. AN1173) can be attributed to the reduced free path for dislocation slip and the weakening in the slip band refinement [43] due to the larger size and the higher volume fraction of coherent κ–carbides after aging. Yield strength is plotted as a function of uniform elongation for all samples in the present study, along with the data for the DUPLEX steels [5], the TRIPLEX steels [3], and the high specific strength steels [15]. It is interesting to note that the present steel shows better tensile properties as compared to the other advanced lightweight steels. Moreover, the aged samples (dash line) display a better synergy of strength and ductility as compared to the unaged samples (solid line), and the corresponding deformation mechanisms will be revealed next.

In our aged samples, various boundaries exist for different domains with dramatic difference in mechanical properties, such as unrecrystallized areas for austenite phase, recrystallized austenite grains, B2 precipitates and κ'–carbides. Due to the accumulated GNDs and strain gradients at these various domain boundaries, HDI hardening should be produced to result in better tensile properties [31,39,40]. In this regard, LUR test have been conducted for the selected samples (one typical unaged sample of AN1173 and the corresponding aged sample of AG1173), the corresponding LUR curves are displayed in Fig. 7a. The typical hysteresis loops with close-up views are shown in Fig. 7b, in which the unloading yield stress (σ_u) and the reloading yield stress (σ_r) can be determined. Then the HDI stress can be calculated based on the equations proposed in our previous paper [39]: $\sigma_{HDI} = (\sigma_u + \sigma_r)/2$). In Fig. 7c, the curves of σ_{HDI} as a function of true strain for these two samples are displayed. It is clearly shown that HDI stress and HDI hardening play a more important role in the aged sample as compared to the corresponding unaged sample, resulting in better tensile properties in the aged sample.

4. Discussions

4.1. Strain hardening mechanisms revealed by EBSD

Generally, HDI hardening can be induced by strain gradients and GNDs produced at various domain boundaries, and the density of GNDs can be related to the KAM value in general using the strain gradient theory [44,45]. Thus, the KAM mappings based on EBSD for the AN1073 sample and the AG1173 sample prior to and after tensile deformation with a same tensile strain (about 6%) are shown in Fig. 8a-d. Then, the corresponding distributions of KAM values prior to and after tensile deformation for the aforementioned two samples are displayed in Fig. 8e and f, and the average values of KAM increments for these two samples are also provided. It is shown that the average values of KAM increments for the recrystallized grains are much larger than those for the un-recrystallized area. This indicates that the plastic deformation is mostly accommodated by the recrystallized grains, and strain

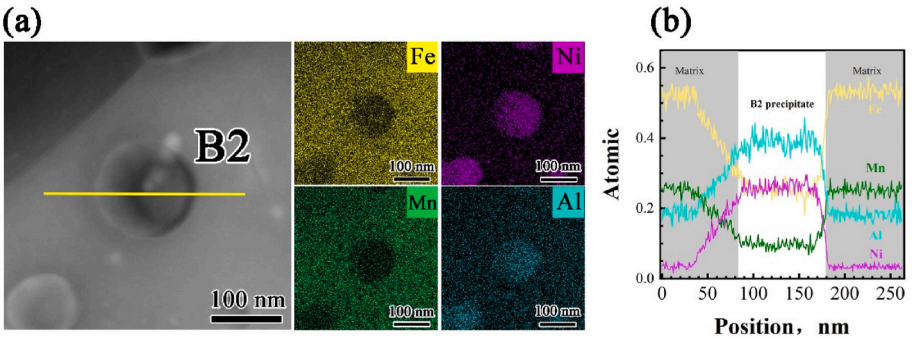

Fig. 5. (a) EDS mappings of an area with several B2 nanoprecipitates for the AG1173 samples. (b) Element distributions along the marked line in (a).

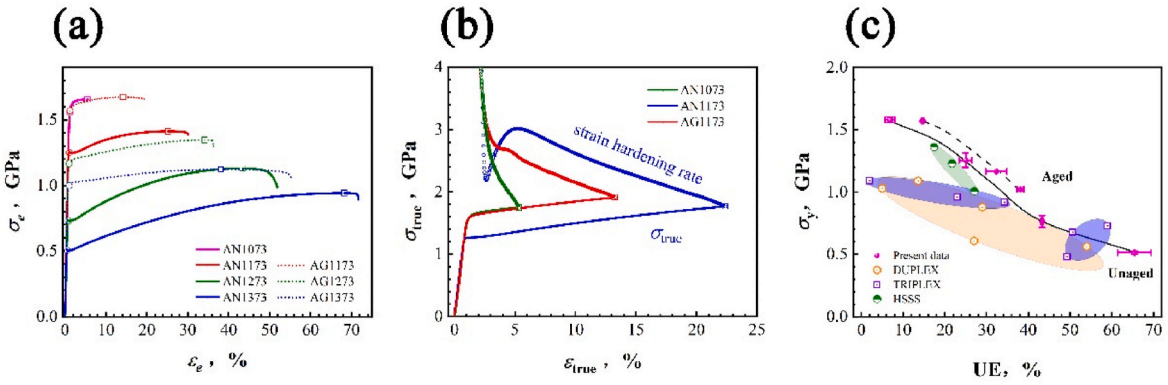

Fig. 6. Tensile properties. (a) Engineering stress-strain curves for selected samples. (b) Hardening rate and true stress as a function of true strain for selected samples. (c) Specific yield strength vs. uniform elongation for all samples in the present study, along with the data for the other lightweight steels [3,5,15].

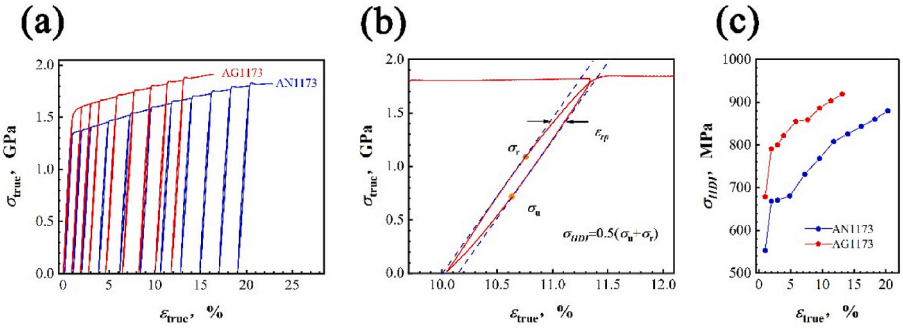

Fig. 7. (a) LUR curves for two typical samples (one unaged sample of AN1173 and the corresponding aged sample of AG1173). (b) Close-up views of typical hysteresis loops showing the determinations for the unloading yield stress (σ_u) and the reloading yield stress (σ_r). (c) σ_{HDI} as a function true strain for the two samples.

partitioning exists between the recrystallized grains and the un-recrystallized area during tensile deformation. It also should be noted that the average value of KAM increments for the AG1173 sample is much larger than that for the AN1073 sample (0.37^0 vs. 0.1^0). Although the deformations of homogeneous structures and heterogeneous structures can both induce the KAM increment, the heterogeneous structures should play a much more important role on the KAM increment. Thus, the aged samples with higher volume fraction of coherent κ'–carbides can produce higher HDI hardening and higher density of GNDs, resulting in better tensile properties. Moreover, the higher ductility of the AG1173 sample (as compared to the AN1073 sample) can't only be attributed to HDI hardening, the nature of higher forest dislocation storage capability of the AG1173 sample with much higher recrystallized area could also play an important role.

4.2. Deformation mechanisms revealed by TEM

The microstructures after tensile deformation for the AG1173 sample were also characterized by TEM and HRTEM, as shown in Figs. 9 and 10, respectively. As indicated in Fig. 9a and b, high density of dislocations can be found in the grain interiors after tensile deformation, especially at the adjacent area of B2 precipitates. Numerous dislocations are pinned by B2 precipitates, and bypassing mechanisms have been revealed for precipitation hardening of B2 precipitates. These B2 particles serve as strain hardening agents by blocking dislocations, resulting in bypassing hardening mechanism. Bypassing precipitation hardening of B2 particles should have great influence on the strain hardening and tensile properties since the size and the interspacing of B2 precipitates are hundreds of nm or less than 100 nm. Stacking faults (SFs) and deformation nanotwins with interspacing at tens of nm can also be observed in the grain interiors, as indicated in Fig. 9c. In general, SFs and deformation nanotwins can be formed more easily in metals with low SF energy (SFE) or medium SFE [46,47]. While, SFs can also be formed due to the high stress induced under high strain rates or at extreme temperatures in metals with high SFE [48,49]. According to the previous paper with a similar material [50], the SFE for this steel should be about 80 mJ/m^2. SFs can be formed in the aged samples, which might be due to the induced high stress because of high density of coherent κ'–carbides with nanoscale in the grain interiors. Dislocation slip can be blocked by SFs and twin boundaries, resulting in strong strain hardening by interaction between them and dislocations.

Dark-field TEM image after tensile deformation for the AG1173 sample is shown in Fig. 10a. HRTEM image after tensile deformation for the AG1173 sample is displayed in Fig. 10b. The images after FFT and inverse FFT are shown in Fig. 10c and e. In Fig. 10e, dislocations are marked by "⊥". The close-up view showing dislocations is given in Fig. 10f. The size distributions prior to and after tensile deformation for the coherent κ'–carbides in the AG1173 sample are displayed in Fig. 10d. It is indicated earlier that the size is larger and the volume fraction is higher for the coherent κ'–carbides in the aged samples compared to the unaged samples, thus the interspacing should be smaller for the coherent κ'–carbides in the aged samples. The interaction mechanism between dislocations and coherent κ'–carbides is clearly shown in Fig. 10e. High density of dislocations can be observed both around and inside the coherent κ'–carbides. Moreover, the dislocation density is found to be significantly higher at the adjacent area of coherent κ'–carbides than that away from them. A shearing precipitation hardening mechanism can be revealed for the interaction between dislocations and coherent κ'–carbides since high density of dislocations can also be found inside coherent κ'–carbides. Thus, the bypassing precipitation hardening mechanism has been revealed for the harder B2 particles, and the softer coherent κ'–carbides can be sheared by

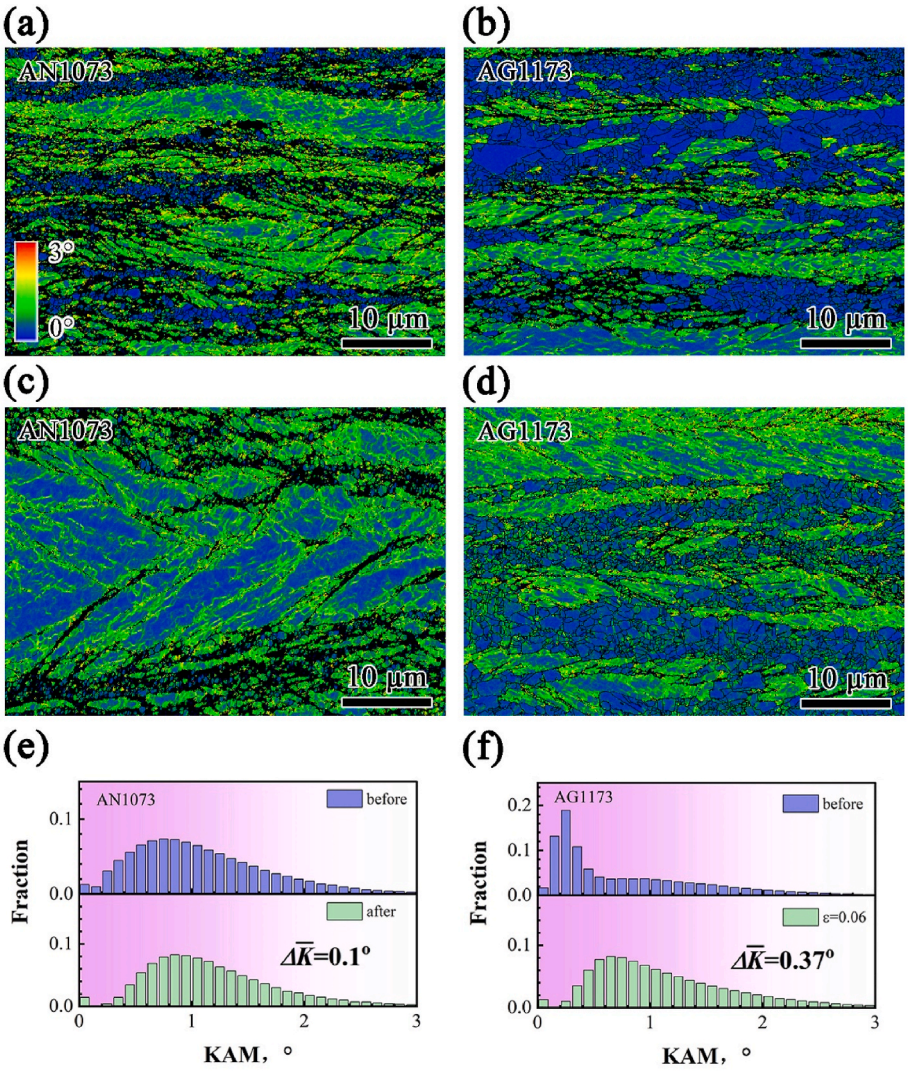

Fig. 8. KAM mappings for the AN1073 sample: (a) prior to tensile testing; (b) after tensile deformation (at a tensile strain of about 6%). KAM mappings for the AG1173 sample: (c) prior to tensile testing; (d) at a tensile strain of about 6%. Histogram distributions of KAM values prior to and after tensile deformation for (e) the AN1073 sample; (f) the AG1173 sample.

dislocations. The average size of coherent κ'–carbides is found to be smaller after tensile deformation as compared to that prior to tensile deformation, due to the shearing hardening mechanism of coherent κ'–carbides. Thus, larger size of coherent κ'–carbides after aging treatment can resist shearing by dislocations and accumulate more dislocations for stronger precipitation hardening. Both precipitation hardening mechanisms can result in strong strain hardening for superior tensile properties. Better tensile properties can be achieved in the aged samples due to the stronger shearing precipitation hardening effect by larger size and higher volume fraction of coherent κ'–carbides, similar to the precipitation hardening effect for the other coherent nanoprecipitates [51, 52].

5. Conclusions

In the present study, Heterogeneous grain structures with dual-nanoprecipitates have been designed and fabricated in a lightweight steel (Fe-29.02Mn-8.76Al-4.99Ni-1.04C) by CR, annealing and aging treatments. And then, the tensile properties and the deformation mechanisms of the aged samples were studied and compared with those of the unaged samples. The concluding remarks are listed as follows:

(1) The aging treatment is found to have little effect on the heterogeneous grain structure and the volume fraction of B2 precipitates. While, the size and the volume fraction of coherent κ'–carbides are found to be much larger/higher after aging treatment.
(2) A better synergy of strength and ductility can be achieved in the aged samples as compared to the unaged samples, which can be attributed to the higher HDI hardening and the higher density of induced GNDs.
(3) Two distinct precipitation hardening mechanisms were revealed for the dual-nanoprecipitates, i.e., bypassing mechanism for B2 precipitates and shearing mechanism for coherent κ'–carbides. Larger size and higher volume fraction of coherent κ'–carbides in the aged samples can result in stronger shearing precipitation hardening effect for better tensile properties.
(4) High density of coherent κ'–carbides at nanoscale can induce high stress in the grain interiors, thus SFs and deformation nanotwins are formed in the aged samples. Strong strain hardening can be achieved by interaction between dislocations and SFs/nanotwins in the aged samples for better tensile properties. The present results should be helpful for achieving excellent

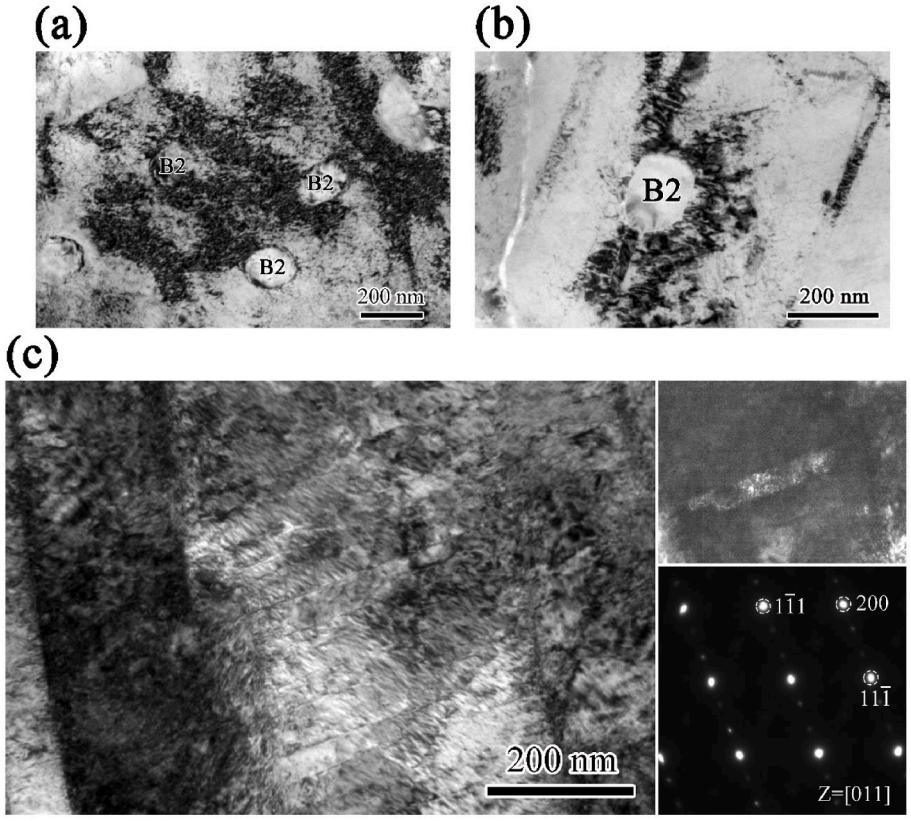

Fig. 9. Bright-field TEM images after tensile deformation for the AG1173 sample.

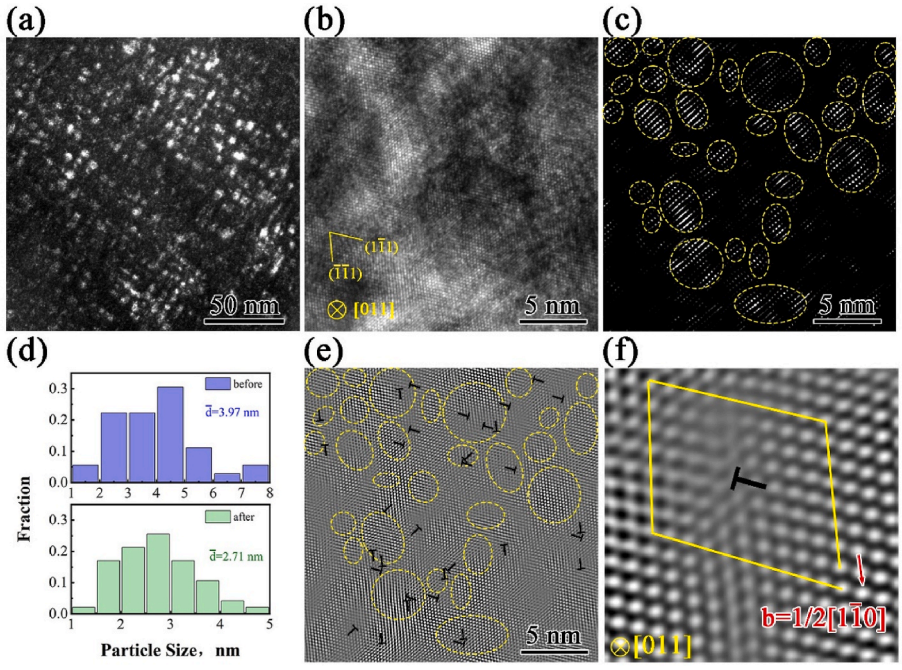

Fig. 10. TEM and HRTEM characterizations after tensile deformation for the AG1173 sample. (a) Dark-field TEM image. (b) HRTEM image. (c)(e) HRTEM images after FFT and inverse FFT. (d) The size distributions prior to and after tensile deformation for the coherent κ'–carbides. (f) Close-up view of HRTEM image showing dislocations.

tensile properties by adjusting microstructures in lightweight steels.

CRediT authorship contribution statement

Jian Wang: Investigation. **Muxin Yang:** Investigation. **Xiaolei Wu:** Conceptualization, Supervision. **Fuping Yuan:** Conceptualization,

Writing – original draft, Supervision.

Declaration of competing interest

The authors declare that they have no known competing financial interests or personal relationships that could have appeared to influence the work reported in this paper.

Data availability

Data will be made available on request.

Acknowledgements

This research was supported by the NSFC Basic Science Center Program for "Multiscale Problems in Nonlinear Mechanics" [grant number 11988102], the National Key R&D Program of China [grant number 2017YFA0204402], the National Natural Science Foundation of China [grant numbers 52192591 and 11790293].

References

[1] W.K. Choo, J.H. Kim, J.C. Yoon, Microstructural change in austenitic Fe-30.0wt% Mn-7.8wt%Al-1.3wt%C initiated by spinodal decomposition and its influence on mechanical properties, Acta Mater. 45 (1997) 4877–4885.
[2] M. Militzer, A synchrotron look at steel, Science 298 (2002) 975–976.
[3] G. Frommeyer, U. Bruex, Microstructures and mechanical properties of high strength Fe-Mn-Al-C light-weight TRIPLEX steels, Steel Res. Int. 77 (2006) 627–633.
[4] J.D. Yoo, S.W. Hwang, K.-T. Park, Factors influencing the tensile behavior of a Fe-28Mn-9Al-0.8C steel, Mater. Sci. Eng., A 508 (2009) 234–240.
[5] Y. Sutou, N. Kamiya, R. Umino, I. Ohnuma, K. Ishida, High-strength Fe-20Mn-Al-C-based alloys with low density, ISIJ Int. 50 (2010) 893–899.
[6] S.W. Hwang, J.H. Ji, E.G. Lee, K.-T. Park, Tensile deformation of a duplex Fe-20Mn-9Al-0.6C steel having the reduced specific weight, Mater. Sci. Eng., A 528 (2011) 5196–5203.
[7] I. Gutierrez-Urrutia, D. Raabe, Multistage strain hardening through dislocation substructure and twinning in a high strength and ductile weight-reduced Fe-Mn-Al-C steel, Acta Mater. 60 (2012) 5791–5802.
[8] H. Springer, D. Raabe, Rapid alloy prototyping: compositional and thermo-mechanical high throughput bulk combinatorial design of structural materials based on the example of 30Mn–1.2C–xAl triplex steels, Acta Mater. 60 (2012) 4950–4959.
[9] H. Kim, D.W. Suh, N.J. Kim, Fe-Al-Mn-C lightweight structural alloys: a review on the microstructures and mechanical properties, Sci. Technol. Adv. Mater. 14 (2013), 014205.
[10] I. Gutierrez-Urrutia, D. Raabe, Influence of Al content and precipitation state on the mechanical behavior of austenitic high-Mn low-density steels, Scripta Mater. 68 (2013) 343–347.
[11] R. Rana, C. Lahaye, R.K. Ray, Overview of lightweight ferrous materials: strategies and promises, JOM 66 (2014) 1734–1746.
[12] D. Raabe, H. Springer, I. Gutierrez-Urrutia, F. Roters, M. Bausch, J.B. Seol, M. Koyama, P.P. Choi, K. Tsuzaki, Alloy design, combinatorial synthesis, and microstructure–property relations for low-density Fe-Mn-Al-C austenitic steels, JOM 66 (2014) 1845–1856.
[13] S.S. Sohn, H. Song, B.C. Suh, J.H. Kwak, B.J. Lee, N.J. Kim, S. Lee, Novel ultra-high strength (ferrite + austenite) duplex lightweight steels achieved by fine dislocation substructures (Taylor lattices), grain refinement, and partial recrystallization, Acta Mater. 96 (2015) 301–310.
[14] Z.Q. Wu, H. Ding, X.H. An, D. Han, X.Z. Liao, Influence of Al content on the strain-hardening behavior of aged low density Fe-Mn-Al-C steels with high Al content, Mater, Sci. Eng. A 639 (2015) 187–191.
[15] S.H. Kim, H. Kim, N.J. Kim, Brittle intermetallic compound makes ultrastrong low density steel with large ductility, Nature 518 (2015) 77–79.
[16] M.X. Yang, F.P. Yuan, Q.G. Xie, Y.D. Wang, E. Ma, X.L. Wu, Strain hardening in Fe-16Mn-10Al-0.86 C-5Ni high specific strength steel, Acta Mater. 109 (2016) 213–222.
[17] S. Chen, R. Rana, A. Haldar, R.K. Ray, Current state of Fe-Mn-Al-C low density steels, Prog. Mater. Sci. 89 (2017) 345–391.
[18] M.J. Yao, E. Welsch, D. Ponge, S.M.H. Haghighat, S. Sandlobes, P. Choi, M. Herbig, I. Bleskov, T. Hickel, M. Lipinska-Chwalek, P. Shanthraj, C. Scheu, S. Zaefferer, B. Gault, D. Raabe, Strengthening and strain hardening mechanisms in a precipitation-hardened high-Mn lightweight steel, Acta Mater. 140 (2017) 258–273.
[19] Z.W. Wang, W.J. Lu, H. Zhao, C.H. Liebscher, J.Y. He, D. Ponge, D. Raabe, Z.M. Li, Ultrastrong lightweight compositionally complex steels via dual-nanoprecipitation, Sci. Adv. 6 (2020), eaba9543.
[20] W. Wang, Y.K. Liu, Z.H. Zhang, M.X. Yang, L.L. Zhou, J. Wang, P. Jiang, F.P. Yuan, X.L. Wu, Deformation mechanisms for a new medium-Mn steel with 1.1 GPa yield strength and 50% uniform elongation, J. Mater. Sci. Technol. 132 (2023) 110–118.
[21] E. Hornbogen, K.-H. Zum Gahr, Distribution of plastic strain in alloys containing small particles, Metallography 8 (1975) 181–202.
[22] J.H. Hwang, T.T.T. Trang, O. Lee, G. Park, A. Zargaran, N.J. Kim, Improvement of strength-ductility balance of B2-strengthened lightweight steel, Acta Mater. 191 (2020) 1–12.
[23] P.V. Liddicoat, X.Z. Liao, Y.H. Zhao, Y.T. Zhu, M.Y. Murashkin, E.J. Lavernia, R. Z. Valiev, S.P. Ringer, Nanostructural hierarchy increases the strength of aluminium alloys, Nat. Commun. 1 (2010) 63.
[24] G. Liu, G.J. Zhang, F. Jiang, X.D. Ding, Y.J. Sun, J. Sun, E. Ma, Nanostructured high-strength molybdenum alloys with unprecedented tensile ductility, Nat. Mater. 12 (2013) 344–350.
[25] T. Yang, Y.L. Zhao, Y. Tong, Z.B. Jiao, J. Wei, J.X. Cai, X.D. Han, D. Chen, A. Hu, J. J. Kai, K. Lu, Y. Liu, C.T. Liu, Multicomponent intermetallic nanoparticles and superb mechanical behaviors of complex alloys, Science 362 (2018) 933–937.
[26] Y.J. Liang, L.J. Wang, Y.R. Wen, B.Y. Cheng, Q.L. Wu, T.Q. Cao, Q. Xiao, Y.F. Xue, G. Sha, Y.D. Wang, Y. Ren, X.Y. Li, L. Wang, F.C. Wang, H.N. Cai, High-content ductile coherent nanoprecipitates achieve ultrastrong high-entropy alloys, Nat. Commun. 9 (2018) 4063.
[27] X.H. Du, W.P. Li, H.T. Chang, T. Yang, G.S. Duan, B.L. Wu, J.C. Huang, F.R. Chen, C.T. Liu, W.S. Chuang, Y. Lu, M.L. Sui, E.W. Huang, Dual heterogeneous structures lead to ultrahigh strength and uniform ductility in a Co-Cr-Ni medium-entropy alloy, Nat. Commun. 11 (2020) 2390.
[28] Y. Yang, T.Y. Chen, L.Z. Tan, J.D. Poplawsky, K. An, Y.L. Wang, G.D. Samolyuk, K. Littrell, A.R. Lupini, A. Borisevich, E.P. George, Bifunctional nanoprecipitates strengthen and ductilize a medium-entropy alloy, Nature 595 (2021) 245–249.
[29] R.Z. Valiev, I.V. Alexandrov, Y.T. Zhu, T.C. Lowe, Paradox of strength and ductility in metals processed bysevere plastic deformation, J. Mater. Res. 17 (2002) 5–8.
[30] M.A. Meyers, A. Mishra, D.J. Benson, Mechanical properties of nanocrystalline materials, Prog. Mater. Sci. 51 (2006), 427–556.
[31] X.L. Wu, M.X. Yang, F.P. Yuan, G.L. Wu, Y.J. Wei, X.X. Huang, Y.T. Zhu, Heterogeneous lamella structure unites ultrafine-grain strength with coarse-grain ductility, Proc. Natl. Acad. Sci. U.S.A. 112 (2015) 14501–14505.
[32] M.X. Yang, D.S. Yan, F.P. Yuan, P. Jiang, E. Ma, X.L. Wu, Dynamically reinforced heterogeneous grain structure prolongs ductility in a medium-entropy alloy with gigapascal yield strength, Proc. Natl. Acad. Sci. USA 115 (2018) 7224–7229.
[33] Y. Ma, F.P. Yuan, M.X. Yang, P. Jiang, E. Ma, X.L. Wu, Dynamic shear deformation of a CrCoNi medium-entropy alloy with heterogeneous grain structures, Acta Mater. 148 (2018) 407–418.
[34] T.H. Fang, W.L. Li, N.R. Tao, K. Lu, Revealing extraordinary intrinsic tensile plasticity in gradient nano-grained copper, Science 331 (2011) 1587–1590.
[35] X.L. Wu, P. Jiang, L. Chen, F.P. Yuan, Y.T. Zhu, Extraordinary strain hardening by gradient structure, Proc. Natl. Acad. Sci. 111 (2014) 7197–7201.
[36] Z. Zeng, X.Y. Li, D.S. Xu, L. Lu, H.J. Gao, T. Zhu, Gradient plasticity in gradient nano-grained metals, Extre. Mech. Lett. 8 (2015) 213–219.
[37] Z. Cheng, H. Zhou, Q. Lu, H. Gao, L. Lu, Extra strengthening and work hardening in gradient nanotwinned metals, Science 362 (2018), eaau1925.
[38] Q.S. Pan, L.X. Zhang, R. Feng, Q.H. Lu, K. An, A.C. Chuang, J.D. Poplawsky, P. K. Liaw, L. Lu, Gradient-cell-structured high-entropy alloy with exceptional strength and ductility, Science 374 (2021) 984–989.
[39] M.X. Yang, Y. Pan, F.P. Yuan, Y.T. Zhu, X.L. Wu, Back stress strengthening and strain hardening in gradient structure, Mater. Res. Lett. 4 (2016) 145–151.
[40] Y.T. Zhu, X.L. Wu, Perspective on hetero-deformation induced (HDI) hardening and back stress, Mater. Res. Lett. 7 (2019) 393–398.
[41] S. Qin, M.X. Yang, P. Jiang, J. Wang, X.L. Wu, H. Zhou, F.P. Yuan, Designing structures with combined gradients of grain size and precipitation in high entropy alloys for simultaneous improvement of strength and ductility, Acta Mater. 230 (2022), 117847.
[42] G. Fribourg, Y. Bréchet, A. Deschamps, A. Simar, Microstructure-based modelling of isotropic and kinematic strain hardening in a precipitation hardened aluminium alloy, Acta Mater. 59 (2011) 3621–3635.
[43] Z.Q. Wu, H. Ding, X.H. An, D. Han, X.Z. Liao, Influence of Al content on the strain-hardening behavior of aged low density Fe–Mn–Al–C steels with high Al content, Mater. Sci. Eng., A 639 (2015) 187–191.
[44] H.J. Gao, Y.G. Huang, W.D. Nix, J.W. Hutchinson, Mechanism-based strain gradient plasticity - I. Theory, J. Mech. Phys. Solid. 47 (1999) 1239–1263.
[45] L.P. Kubin, A. Mortensen, Geometrically necessary dislocations and strain-gradient plasticity: a few critical issues, Scripta Mater. 48 (2003) 119–125.
[46] Y. Ma, M.X. Yang, F.P. Yuan, X.L. Wu, Deformation induced hcp nano-lamella and its size effect on the strengthening in a CoCrNi medium-entropy alloy, J. Mater. Sci. Technol. 82 (2021) 122–134.
[47] P. Ren, X.P. Chen, C.Y. Wang, Y.X. Zhou, W.Q. Cao, Q. Liu, Evolution of microstructure, texture and mechanical properties of Fe-30Mn-11Al-1.2C low-density steel during cold rolling, Mater. Char. 174 (2021), 111013.
[48] F. Zhao, L. Wang, D. Fan, B.X. Bie, X.M. Zhou, T. Suo, Y.L. Li, M.W. Chen, C.L. Liu, M.L. Qi, M.H. Zhu, S.N. Luo, Macrodeformation twins in single-crystal aluminum, Phys. Rev. Lett. 116 (2016), 075501.
[49] M.W. Chen, E. Ma, K.J. Hemker, H.W. Sheng, Y.M. Wang, X.M. Cheng, Deformation twinning in nanocrystalline aluminum, Science 300 (2003) 1275–1277.

[50] Z.W. Wang, W.J. Lu, F.C. An, M. Song, D. Ponge, D. Raabe, Z.M. Li, High stress twinning in a compositionally complex steel of very high stacking fault energy, Nat. Commun. 13 (2022) 3598.
[51] Z.H. Zhang, P. Jiang, F.P. Yuan, X.L. Wu, Enhanced tensile properties by heterogeneous grain structures and coherent precipitates in a CoCrNi-based medium entropy alloy, Mater. Sci. Eng., A 832 (2022), 142440.
[52] S. Qin, M.X. Yang, P. Jiang, J. Wang, X.L. Wu, H. Zhou, F.P. Yuan, Designing structures with combined gradients of grain size and precipitation in high entropy alloys for simultaneous improvement of strength and ductility, Acta Mater. 230 (2022), 117847.